



# Ionic-liquid-assisted synthesis of high-visible-light-activated N–B–F-tri-doped mesoporous TiO<sub>2</sub> via a microwave route



Fa-tang Li <sup>a,\*</sup>, Xiao-jing Wang <sup>a</sup>, Ye Zhao <sup>a</sup>, Ji-xing Liu <sup>a</sup>, Ying-juan Hao <sup>a</sup>, Rui-hong Liu <sup>a</sup>, Di-shun Zhao <sup>b</sup>

<sup>a</sup> College of Science, Hebei University of Science and Technology, Shijiazhuang, China

<sup>b</sup> College of Chemical and Pharmaceutical Engineering, Hebei University of Science and Technology, Shijiazhuang, China

## ARTICLE INFO

### Article history:

Received 3 May 2013

Received in revised form 15 July 2013

Accepted 21 July 2013

Available online 30 July 2013

### Keywords:

N–B–F-tri-doped TiO<sub>2</sub>

Ionic liquid

Mesoporous materials

Photocatalysis

Visible light

## ABSTRACT

A facile and green method was developed for the simultaneous doping of nitrogen, boron, and fluorine in TiO<sub>2</sub> by H<sub>2</sub>TiO<sub>3</sub> via a microwave-assisted route. The ionic liquid (IL) [BmIm]BF<sub>4</sub> serves not only as microwave absorbent but also as a dopant. The IL also shows the ability to self-assemble under microwave irradiation, which causes it to act as an inhibitor for the growth of the TiO<sub>2</sub> particles. The N–B–F-tri-doped TiO<sub>2</sub> obtained exhibits large specific surface area, small crystal size, and a mesoporous structure, and the mechanism for the formation of the N–B–F-tri-doped TiO<sub>2</sub> was proposed. The prepared materials exhibit excellent visible light photocatalytic activity in the degradation of organic pollutants, including methyl orange, rhodamine B, Orange G, and reactive red X, which is attributed to the presence of a Ti–B–N structure on the TiO<sub>2</sub> surface, inducing a narrow band gap of 2.78 eV, and the synergistic effects of N, B, and F, which improve the separation efficiency of the photo-generated electron/hole pairs. The results obtained may provide a new sight for the application of ILs in the microwave-assisted preparation of nanomaterials.

© 2013 Elsevier B.V. All rights reserved.

## 1. Introduction

The applications of TiO<sub>2</sub> in solar cells, environmental purification, H<sub>2</sub>-generation, and self-cleaning have received extensive attention due to the attractive attributes of TiO<sub>2</sub>, including its strong oxidizing abilities for the decomposition of organic pollutants, chemical and biological stability, non-toxicity, and low cost [1]. Because anatase TiO<sub>2</sub> can only absorb UV light of wavelengths less than 387 nm, which accounts for only approximately 4% of the solar spectrum impinging on the Earth's surface compared to visible light (45%), considerable effort has been devoted to extend the optical absorption edge of TiO<sub>2</sub> from the UV to visible light region to utilize solar energy more effectively for photocatalysis, which will have a profound positive effect on the practical applications of the material [2]. An effective approach to tackle the challenge is to dope TiO<sub>2</sub> with nonmetal elements such as N [3–6], B [7–9], C [10], S [11], and F [12,13], which act as either electron donors or acceptors in the forbidden band of TiO<sub>2</sub>, thus, inducing absorption in the visible region [14]. This modification is sensitive and affected by both the chemical state and spatial distribution of the anion dopants [15,16], and only the bulk doping of substitutional dopants for lattice oxygen can result in the desired band

gap narrowing by elevating the valence band edge of the photocatalyst. Unfortunately, new recombination centers associated with dopants are always formed in the doped photocatalyst because of the charge balance requirement (for instance, nitrogen-related Ti<sup>3+</sup> in N-doped TiO<sub>2</sub> [17]). Compared with a single nonmetal dopant, doping with two or three types of nonmetal atoms, such as N and S [18–20]; N and C [21]; N and F [22–24]; N and B [8,25–27]; N and I [28]; and N, C and S [29] has served as an attractive approach due to the lower charge carrier recombination rate and higher visible photocatalytic performance resulting from the synergistic effect of the doping elements. For example, Liu et al. [26,30] reported the preparation of mesoporous B–N-co-doped TiO<sub>2</sub> with significantly enhanced visible-light adsorption and photocatalytic activity. These observations were attributed to the presence of a new O–Ti–B–N structure formed on the surface of the photocatalyst, which is highly active in collecting and separating the charge carriers. Due to the charge compensation effect of the nitrogen and boron anions, no new recombination centers (such as Ti<sup>3+</sup>) of electrons and holes were formed, which inhibits the decrease of photocatalytic activity. Li et al. [31] also prepared F–B–S-tri-doped TiO<sub>2</sub> thin films by a modified sol–gel method and proposed that the synergistic effect of the F<sup>–</sup>, B<sup>3+</sup> and S<sup>4+</sup> ions reduced the recombination of the photo-generated electrons and holes and enhanced the photoreactivity.

To achieve high-efficiency, nonmetal doping of TiO<sub>2</sub>, several approaches have been proposed, including the sol–gel method

\* Corresponding author. Tel.: +86 311 81669971; fax: +86 311 81668528.  
E-mail address: [lifatang@126.com](mailto:lifatang@126.com) (F.-t. Li).

[31], high-temperature calcination in a special gas atmosphere (for example, N<sub>2</sub> or NH<sub>3</sub>) [32], a hydrothermal method [21,33], compound pyrolysis [34], sputtering using a high-energy ion gun [35], and a microwave-assisted process [36]. Among them, microwave-assisted synthesis is a facile, highly efficient and environmentally friendly method. In the past two decades, the use of microwave energy to heat chemical reactions has attracted considerable attention, owing to its successful application in material sciences, nano-technology, polymer chemistry, and biochemical processes [37]. In the microwave process, ionic liquids (ILs) have been widely used as reaction media owing to their unique properties, such as excellent ability to absorb microwave irradiation, non-volatility, non-flammability, wide liquid temperature range, good solubility characteristics, high thermal stability, and high ionic conductivity [38,39]. In recent years, many inorganic nanostructures have been fabricated via various processes using ILs, including electrodeposition, the sol–gel method and the solvothermal route. Ding et al. [38] reported a facile method to synthesize anatase nanocrystals (NCs) via a microwave-assisted route in the IL 1-butyl-3-methylimidazolium tetrafluoroborate ([BMIm]BF<sub>4</sub>) using titanium isopropoxide (TTIP) as the titanium source without calcination. Using this method, there was no porous structure and almost no visible light absorption was observed for the nano-TiO<sub>2</sub> powders obtained.

On the other hand, porous materials with a tailored pore size have shown great potential in gas conversion and storage, catalysis, sensors, adsorption, separation, and biomedical applications [40–43]. These materials have regular pore structures, which are useful for adsorption, selection, sensing, removal, storage, and release as well as properties based on their enhanced surface areas [44]. In photocatalysis, porous materials have a high capacity for dye adsorption because of the internal surface area provided by the primary single nanocrystallites [45], which benefits the subsequent catalysis process.

Herein, we report a facile method to synthesize nitrogen, boron, and fluorine-tri-doped mesoporous TiO<sub>2</sub> using H<sub>2</sub>TiO<sub>3</sub> via a microwave-assisted route. In this study, [BMIm]BF<sub>4</sub> served not only as the microwave absorbent but also as the dopant providing B and F anions. Furthermore, the ability of the IL to self-assemble during the microwave process was discovered, which made the IL act as inhibitor for the growth of the TiO<sub>2</sub> particles and favored the formation of small TiO<sub>2</sub> crystal particles. Because investigations into tri-doping, especially relating to N–B–F-tri-doped TiO<sub>2</sub>, are rather rare, the visible light responsive mechanism of the N–B–F-tri-doped TiO<sub>2</sub> was also discussed. We hope this research can display a new application for ILs in the microwave-assisted preparation of nanomaterials and supports the development of anion-doped TiO<sub>2</sub> with high visible light photocatalytic ability.

## 2. Experimental

### 2.1. Materials

All of the chemicals were used as received without further purification. H<sub>2</sub>TiO<sub>3</sub> was produced by Xuan Cheng Jing Rui New Material Co., Ltd. [BMIm]BF<sub>4</sub> (purity > 99%) was purchased from the Lanzhou Institute of Chemical Physics, Chinese Academy of Sciences. P25 TiO<sub>2</sub> was purchased from Degussa Corp., Germany. All of the other chemical reagents were purchased from Aladdin Chemical Reagent Corp.

### 2.2. Preparation of catalysts

TiO<sub>2</sub> was formed through the media product of peroxotitanate. To prepare peroxotitanate, 1.0 g of H<sub>2</sub>TiO<sub>3</sub> was added to an

ice-cooled solution containing H<sub>2</sub>O, H<sub>2</sub>O<sub>2</sub> (30%) and NH<sub>3</sub>·H<sub>2</sub>O (28%). After stirring for 30 min, a homogeneous, pale yellow-green solution was obtained. Then, a given amount of [BMIm]BF<sub>4</sub> was added to the solution. After stirring continuously for 30 min, the solution was transferred into a flask and microwave irradiated for 1 h. During the reaction, the power and the temperature of the microwave oven (XH-100B, Beijing Xianghu Science and Technology Development Co., Ltd.) were set at 500 W and 80 °C, respectively. After irradiation, the products were separated by filtration and then dried at 80 °C. The samples obtained were calcined at 300–600 °C in a muffle furnace for 2 h. The amount of the IL used was 0, 1, 3, 5, and 10 g, corresponding to weight ratios of the IL/H<sub>2</sub>TiO<sub>3</sub> of 0, 1, 3, 5, and 10, respectively. The photocatalysts obtained with the addition of the corresponding IL were denoted as nTAx, where n and x represent the weight ratio of IL/H<sub>2</sub>TiO<sub>3</sub> and the microwave or calcination temperature (°C), respectively. To observe the difference between the titanium isopropoxide (TTIP) and H<sub>2</sub>TiO<sub>3</sub> precursors in the synthesis of TiO<sub>2</sub>, TTIP was also used to prepare TiO<sub>2</sub> via a microwave-assisted route in [BMIm]BF<sub>4</sub> according to Ref. [38] (this TiO<sub>2</sub> was obtained after calcination at 400 °C and was denoted as ETA400).

### 2.3. Samples characterization

X-ray diffraction (XRD) analysis was carried out using a Rigaku D/MAX 2500 X-ray diffractometer using CuK $\alpha$  radiation. Fourier transform infrared (FT-IR) spectra were obtained using a Shimadzu IR Prestige 21 spectrometer. The Brunauer–Emmett–Teller (BET) specific surface areas (SBET) were measured using a Quantachrome NOVA2000 nitrogen adsorption/desorption apparatus. The X-ray photoelectron spectroscopy (XPS) analysis was carried out using a PHI 1600 ESCA XPS system. Transmission electron microscopy (TEM) and high resolution electron microscopy (HRTEM) images were taken with a JEOL JEM-2010 electron microscope. The UV–vis diffuse reflectance spectra (DRS) were recorded at room temperature between 200 and 800 nm using a Shimadzu UV2450 spectrophotometer. The photoluminescence (PL) spectra of the TiO<sub>2</sub> samples were measured using a Hitachi F-4600 fluorescence spectrophotometer to observe the combination rates of the electron–hole pairs. Electron spin resonance (ESR) measurements were carried out on a Bruker EMX-8/2.7 X-band ESR spectrometer operating in the X-band at 9.86 GHz and 2.005 mW. Portions of the solid samples ( $\approx$ 20 mg) were introduced into a spectroscopic quartz probe cell, and measurements were taken at room temperature.

### 2.4. Photocatalytic activity tests

Three anionic dyes, methyl orange (MO, 10 mg/L), Orange G (OG, 10 mg/L), reactive red X-3B (RX, 30 mg/L), and the cationic dye rhodamine B (RhB, 20 mg/L) were chosen as pollutants to evaluate the activity of the photocatalysts. A 200-mL aqueous solution was mixed with 0.20 g of the photocatalyst powder in a 500-mL beaker. Prior to the photocatalytic reaction, the suspension was stirred in darkness for 30 min to reach adsorption/desorption equilibrium. Irradiation was performed with a 300 W xenon arc lamp that was installed in light-condensing lamp housing, and a 400-nm cut-off filter was placed in front of the reaction vessel to obtain the visible light. The light intensity of the lamp was 0.16 kW/m<sup>2</sup> at 420 nm, which was measured by a light intensity meter. At given time intervals, a 5-mL sample of the suspension was centrifuged and filtered through a 0.22  $\mu$ m Millipore filter to remove the photocatalyst. To investigate the stability of the used photocatalyst, the nanopowders were separated from solution by centrifugation at 13,000 r/min for 4 min and then dried in drying oven at 120 °C for 2 h. Then, the concentration of the pollutants in the sample was analyzed. The

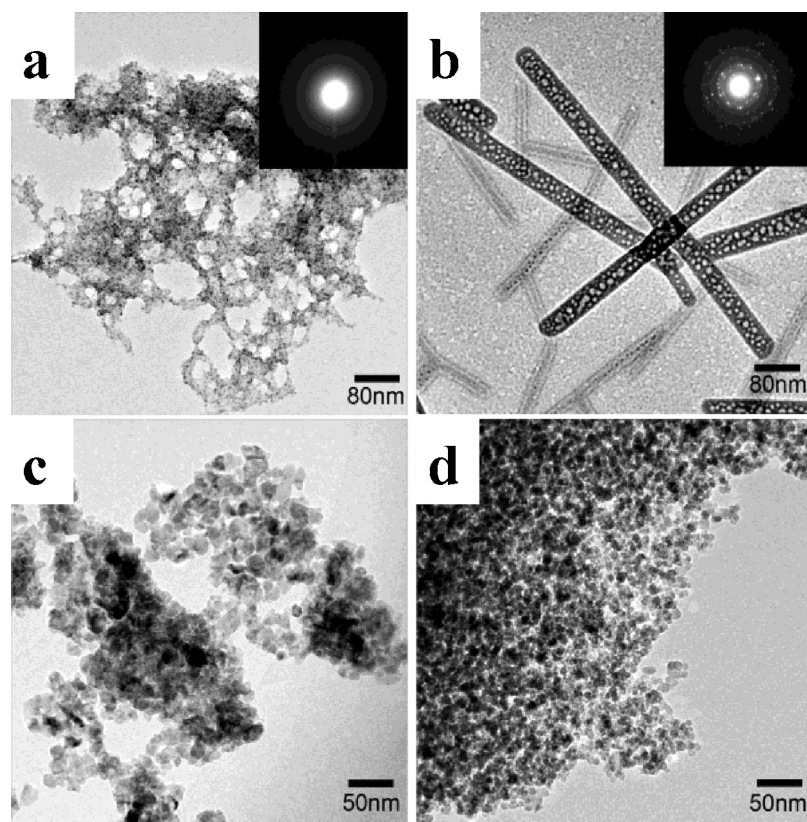


**Fig. 1.** TEM images of samples (a) OTA80, (b) 3TA80, (c) OTA400, and (d) 3TA400.

concentration of pollutants was determined from its maximum absorption, which varied during the photocatalytic process, using a UV-Vis spectrophotometer. The decoloration rate was reported as  $C/C_0$ , where  $C$  was the pollutant concentration after adsorption or photocatalysis and  $C_0$  was the initial concentration. The total organic carbon (TOC) content of the samples after degradation was measured using a Shimadzu TOC-V WS analyser.

#### 2.5. Determination of reactive species

To detect the active species generated in the photocatalytic system, various scavengers, including tert-butyl alcohol (t-BuOH, 20 mmol L<sup>-1</sup>), AgNO<sub>3</sub> (5 mmol L<sup>-1</sup>) and ethylenediaminetetraacetic acid disodium salt (EDTA-2Na, 1 mmol L<sup>-1</sup>), were introduced into the MO solution. Furthermore, to estimate the relative concentration of hydroxyl radicals (•OH radicals), the terephthalic acid (TA) fluorescence method was used because TA can react with •OH radicals to form highly fluorescent 2-hydroxyterephthalic acid (TAOH), which can be detected in a fluorescence spectrum [46]. The experimental procedures were as follows: TA was dissolved in 2.0 mM NaOH to form a 0.5 mM solution [47]. Then, 0.20 g of the 3TA400 sample was dispersed in 200 mL of the TA aqueous solution. The mixture was irradiated under visible light for 30 min. The fluorescence spectra of the TAOH generated were measured on a Hitachi F-4600 fluorescence spectrophotometer at 425 nm induced at 315 nm excitation. ESR/DMPO (dimethyl-1-pyrroline N-oxide) spin trapping experiments were also used to detect the active oxygen species in the system under visible light irradiation [48]. ESR spectra were detected using a Bruker EMX-8/2.7 X-band ESR spectrometer operating in the X-band at 9.86 GHz and 2.005 mW. The light source for the ESR determination was a 300-W xenon lamp equipped with a 400-nm cut-off filter.

### 3. Results and discussion

#### 3.1. Morphology and phase structures

To observe the morphologies of the synthesized TiO<sub>2</sub>, the TEM spectra of representative samples of OTA80 and 3TA80 (without calcination) and OTA400 and 3TA400 (calcined at 400 °C) are shown in Fig. 1a-d, respectively. The insets of Fig. 1a and b show the corresponding selected area electron diffraction (SAED) patterns of OTA80 and 3TA80. As seen in the SAED image in Fig. 1a, after microwave irradiation, the obtained material exhibits an amorphous structure. However, with the addition of the IL, the SAED result indicates that the material was polycrystalline, indicating that the IL is beneficial to the formation of crystals because of its good microwave absorption ability. The XRD patterns shown in Fig. 2 verify the amorphous structure of the sample without the IL (OTA80) and the anatase TiO<sub>2</sub> crystal structure of the sample with the IL (3TA80). Furthermore, the TEM image in Fig. 1b shows that the liquid IL arrays to form nanorods and TiO<sub>2</sub> nanoparticles that are inlayed in the IL phase. It is thought that [BMIm]<sup>+</sup> interacts with the bulk TiO<sub>2</sub> through hydrogen bonds or electrostatic forces, and the nano-TiO<sub>2</sub> particles are wrapped in the IL. This process would induce the arrangement of the [BF<sub>4</sub>]<sup>-</sup> anions along the wall, which would pile up and stack, possibly through π-π interactions or other noncovalent interactions between the imidazole rings [49]. The phenomenon indicates that the IL has the ability to self-assemble during microwave irradiation.

Fig. 1c and d shows the TEM images of the prepared TiO<sub>2</sub> nanoparticles calcined at 400 °C without or with the addition of the IL. After being calcined, the crystal size of the pure TiO<sub>2</sub> sample without the addition of the IL is large, and its dispersion is very poor. However, the crystal sizes of the TiO<sub>2</sub> synthesized assisted by the IL (all approximately 10 nm in size) are smaller on average

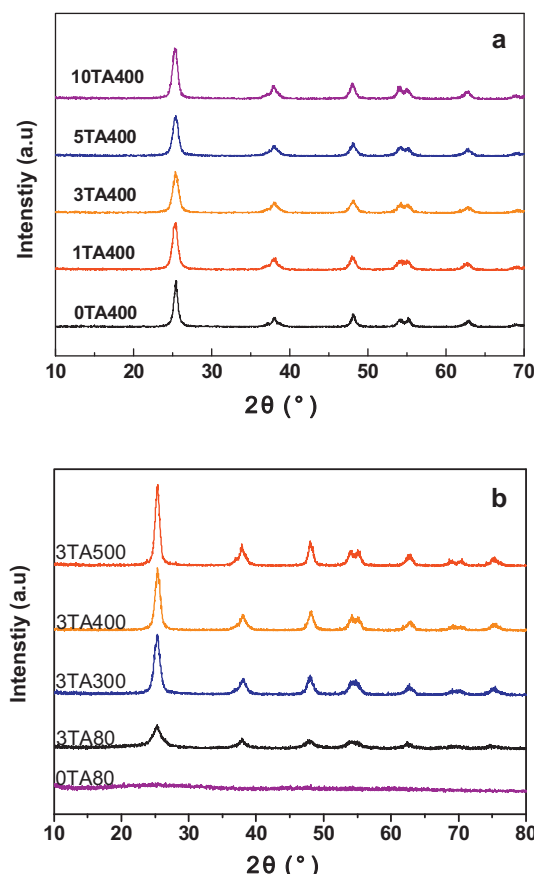


**Fig. 2.** XRD pattern of the  $\text{TiO}_2$  samples. (a) TA400 with different amounts of the IL dopant and (b) 3TA calcined at different temperatures.

and display better dispersion than those of the pure  $\text{TiO}_2$  (approximately 15 nm in size) synthesized without the addition of the IL. The SEM images of the OTA400 and 3TA400 powders were also collected, as shown in Fig. S1. These images indicate that 3TA400 is made up of regularly shaped aggregations with sizes centered approximately 10 nm, and OTA400 is made up of irregularly shaped aggregations. The sizes of the  $\text{TiO}_2$  particles are larger than those of 3TA400. The SEM results are consistent with the TEM results. It is also obvious that the addition of the IL restrains the growth of the  $\text{TiO}_2$  particles, possibly because of its ability to self-assemble.

To investigate the crystalline phases and crystal sizes of the prepared  $\text{TiO}_2$ , the XRD patterns of the  $\text{TiO}_2$  particles calcined at 400 °C for 2 h with different amounts of the IL are shown in Fig. 2a. It is found that all of the diffraction peaks can be perfectly indexed as the anatase phase of  $\text{TiO}_2$  [JCPDS No. 21-1272]. Based on the line-width analysis of the anatase (101) diffraction peak, the average crystal sizes of all of these samples estimated by the Scherer equation are summarized in Table 1. As seen in Table 1, the crystal sizes of the  $\text{TiO}_2$  slightly decreased with the addition of the IL, except

for 10TA400, which indicates that the addition of the IL confined the growth of the  $\text{TiO}_2$  nanoparticles. This result indicates that the IL acted as an inhibitor for the growth of the anatase nanocrystals, which is also consistent with the TEM result, as shown in Fig. 1c and d. In the present experiment, the IL not only acted as a protective agent for the growth of the nanoparticles but also as a microwave absorbant. Because of the strong ability of the superfluous IL to absorb microwave irradiation, 10TA400 leads to the cross-linking of peroxotitanate and the fast growth of the  $\text{TiO}_2$  nanoparticles, resulting in large crystal sizes.

Fig. 2b shows the effect of the calcination temperature on the phase structure change of 3TA80. Only the anatase phase is observed with the increase of the calcination temperature from 300 to 500 °C, while the crystal sizes of the  $\text{TiO}_2$  slightly increased with the increase of the calcination temperature.

### 3.2. Nitrogen physical adsorption

The surface area and porosity distribution of 3TA and OTA calcined at 400 °C were investigated using nitrogen adsorption and desorption isotherms (Fig. S2). The  $S_{\text{BET}}$  values of these prepared samples are all above 80  $\text{m}^2/\text{g}$ , which are much higher than that of P25. The isotherms of the samples are typical type-IV-like with a type H3 hysteretic loop, which indicates the presence of mesoporous materials, according to IUPAC classification [50,51]. The plot of the pore size distribution (inset in Fig. S2) was determined by using the Barrett–Joyner–Halenda (BJH) method from the desorption branch of the isotherm; it shows that all of the samples clearly have a mesoporous structure. The average pore diameter of 3TA400 is approximately 8.50 nm. However, compared to the 3TA400 sample, the area of the hysteretic loop of OTA400 decreases with an average pore diameter of only 3.87 nm. The mesoporous structure of OTA is most likely formed by the release of  $\text{NH}_3$  during calcination, and that of 3TA is formed by both the release of  $\text{NH}_3$  and the agglomeration of primary particles (interparticle pores) due to the combustion and decomposition of the IL. There is no obvious peak at approximately 1.0° in the small-angle XRD patterns (not shown), indicating that the mesoporous structure in 3TA400 is the result of disorder. Table 1 also shows the effect of the amount of the IL on the  $S_{\text{BET}}$  of the samples. With an increase in the addition of the IL, the  $S_{\text{BET}}$  increases first and then decreases when superfluous IL is added, which is consistent with the XRD results.

### 3.3. XPS analysis

XPS measurements were performed to further elucidate the influence of the IL on the doping of the  $\text{TiO}_2$ . The compositions of the photocatalysts are listed in Table 2. The nitrogen, boron and fluorine most likely come from the ammonia and  $[\text{BF}_4]^-$  starting materials. As seen in Table 2, the content of nitrogen, boron and fluorine in the  $\text{TiO}_2$  increased with the addition of the IL, especially for 10TA400. Livraghi reported that  $\text{F}^-$  ions substitute oxygen in the lattice of  $\text{TiO}_2$ , which favors the incorporation of N species in the  $\text{TiO}_2$  and leads to higher N content than in  $\text{N-TiO}_2$  [52]. In this

**Table 1**  
Crystal sizes, energy band gaps,  $S_{\text{BET}}$  values and pore parameters of the samples.

Sample	Crystal size (nm)	$E_g$ (eV)	$S_{\text{BET}}$ ( $\text{m}^2/\text{g}$ )	Average pore size (nm)	Pore volume ( $\text{cm}^3/\text{g}$ )
OTA400	16.9	3.08	87.85	3.87	0.1143
1TA400	11.7	2.85	90.21	8.32	0.2637
3TA400	10.5	2.78	99.71	8.50	0.2799
5TA400	10.6	2.75	112.9	7.90	0.3003
10TA400	13.3	2.92	102.8	7.81	0.2933
3TA300	9.30	–	83.25	4.67	0.1140
3TA500	12.5	3.00	90.32	7.21	0.2562
P25	24.8	3.22	46.48	11.57	0.1405

**Table 2**

The compositions of the photocatalysts measured by XPS.

Sample	Composition (at%)					
	Ti	O	F	N	B	C
0TA400	20.48	59.34	–	1.39	–	18.79
1TA400	21.3	56.19	0.91	1.55	2.44	17.61
3TA400	21.43	54.17	0.96	1.65	2.61	19.18
5TA400	20.81	53.9	1.58	1.71	2.67	19.33
10TA400	20.66	53.19	2.1	2.19	2.75	19.11
3TA500	21.91	56.61	0.26	1.33	3.16	16.73

study, we propose that the increase in N content in 10TA400 may contribute to the substitution of more  $F^-$  ions for oxygen in the lattice of the  $TiO_2$ .

To further investigate the states of the doped nitrogen, boron and fluorine atoms, high resolution and curve fitting of the photocatalysts were recorded and are shown in Fig. 3. A pair of N1s features is observed in Fig. 3a. A broad peak extending from 393 to 406 eV is observed for all of the samples, which is typical of nitrogen-doped titanium dioxide, as reported by several researchers. After fitting the curve, two peaks are obtained at 401.1 eV and 399.6 eV for every sample. However, a weak peak approximately 398.0 eV is obtained in 3TA400; the intensity of this peak increased with increasing addition of the IL (Fig. S3). The peak approximately 401 eV is attributed to the O–Ti–N sites substitutionally incorporated into the  $TiO_2$  lattice [29,53,54]. The peak at 399.6 eV can be attributed to the N atoms located at the interstitial sites of the  $TiO_2$  lattice, such as Ti–N–O and Ti–O–N [53,54]. According to the earlier reports [26,55], the peak at 398.0 eV can be attributed to O–Ti–B–N. The results that show that the N content of 3TA500 is lower than that of 3TA400 and the peak approximately 398.0 eV disappears indicate that the O–Ti–B–N decomposes under increased calcination temperatures.

Fig. 3b shows the F1s XPS spectra of the samples. The peak at 684.2 eV is obtained in every sample; however, the peak at 687.1 eV is only in 10TA400. The peak at 684.2 eV can be assigned to the physical adsorption of F ions on the surface of the  $TiO_2$  [12]. The peak at 687.1 eV can be attributed to the substitutional F atoms that occupy the oxygen sites in the  $TiO_2$  crystal lattice and then form the Ti–O–F bond [12]. The appearance of the peak at 687.1 eV for 10TA400 indicates that the superfluous IL dopant can lead to the replacement of O atoms by F atoms in the crystal lattice. In addition, the decrease of the peak at 684.2 eV with the increase in the calcination temperature indicates that the physical adsorbance of F ions on the surface of the  $TiO_2$  is temperature sensitive.

The XPS spectra of B1s in 3TA400, 10TA400, 3TA500 and ETA400 are shown in Fig. 3c. There are two peaks at 190.5 and 191.5 eV, and the peaks at 187.5 and 193.0 eV, corresponding to B–O from  $B_2O_3$  and the B–Ti bond in  $TiB_2$ , respectively, are not found in these samples. The binding energy (BE) at 190.5 eV is assigned to the B–N bond [56], which corresponds to a species capable of inducing the unprecedented visible light photocatalytic activity [57]. The peak at 191.5 eV may be assigned to the B atom in the interstitial position of the  $TiO_2$  and the formation of a B–O–Ti bond [58,59]. For comparison, the high resolution and curve fitting of the B1s region in ETA400, which was prepared from TTIP in  $[BmIm]BF_4$ , are also recorded. As shown in Fig. 3c, there is only a peak at 191.5 eV, and no peak at 190.5 eV is observed, which shows that the  $TiO_2$  prepared from TTIP cannot form the B–N bond.

It has been reported that in doping  $TiO_2$  with B or N alone, more tri-valent  $Ti^{3+}$  species will form and lead to a slight red shift of the  $Ti2p_{3/2}$  peak [60]. The formation of  $Ti^{3+}$  species in the doped  $TiO_2$  may accelerate the recombination of the photogenerated holes and electron pairs [60]. Recently, Feng et al. reported that the  $Ti2p_{3/2}$  peak of the B–N-co-doped  $TiO_2$  shifted to higher BE compared to

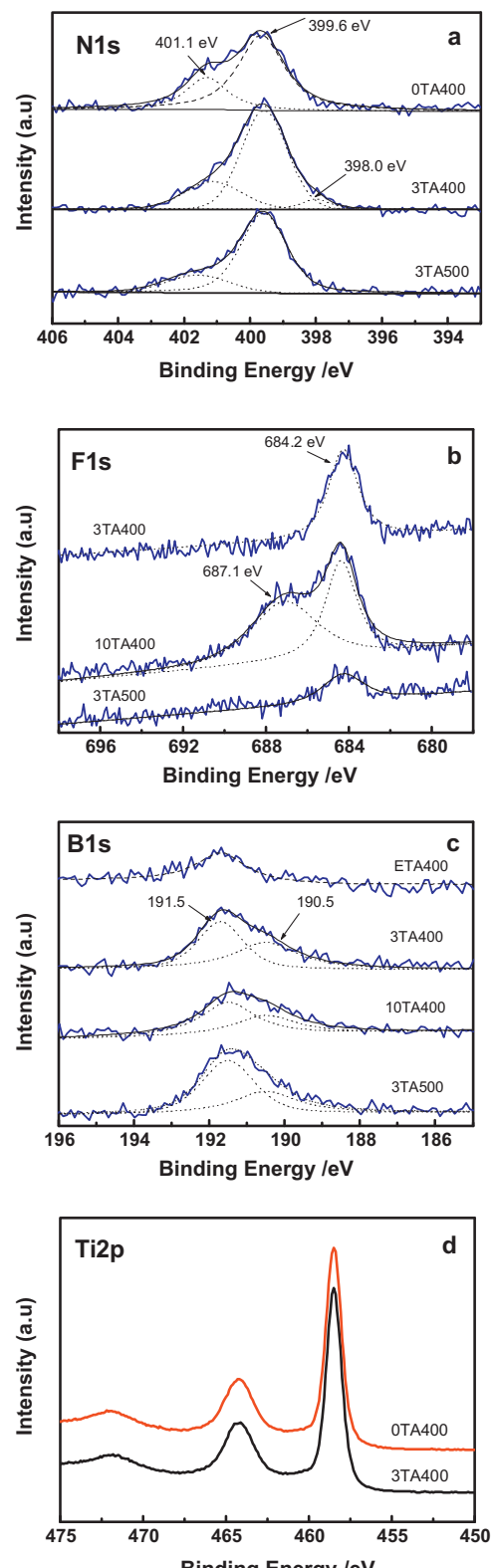


Fig. 3. XPS spectra: (a) N1s, (b) F1s, (c) B1s, and (d) Ti2p of representative samples.

that of the solely B- or N-doped  $TiO_2$ , implying that B–N-co-doping can hinder the conversion of Ti species from  $Ti^{4+}$  to  $Ti^{3+}$  [61]. However, only two peaks were observed at 464.28 eV and 458.48 eV in 0TA400 and 3TA400, which are assigned to  $Ti2p_{1/2}$  and  $Ti2p_{3/2}$ , respectively, agreeing well with the Ti(IV) in titanium. No trace shift of the  $Ti2p_{3/2}$  peak is observed using XPS, although  $Ti^{3+}$  is observed

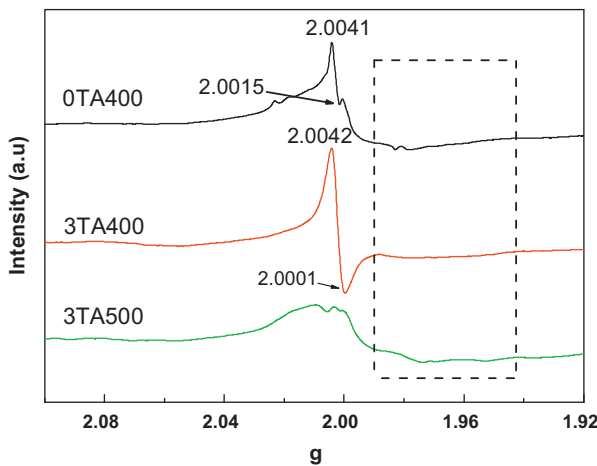


Fig. 4. ESR spectrum of samples measured at room temperature.

in OTA400 using ESR spectroscopy (see Fig. 4). This observation may be attributed to the low amount of  $\text{Ti}^{3+}$ , which is hard to detect by XPS [28,62].

### 3.4. ESR spectra analysis

To further confirm whether  $\text{Ti}^{3+}$  was present in the  $\text{TiO}_2$  samples, ESR studies were performed. Fig. 4 shows the ESR spectra of OTA400, 3TA400 and 3TA500 recorded at room temperature. The symmetric signal at approximately  $g=2.0041$  is clearly detected both in OTA400 and 3TA400. It is the most prominent electron signal and is characteristic of paramagnetic materials containing “F-centers” or oxygen vacancies [28]. Compared to the only sharp signal at approximately  $g=2.0041$  in 3TA400, an additional weak signal at  $g=1.9766$  appears in the OTA400. Previous ESR studies suggest that signals with  $g$  values of less than 2.0 can be attributed to photogenerated electrons stabilized by Ti cations located at the crystallization defects [63,64]. It was also reported that the paramagnetic oxygen vacancy at  $g=2.004$  and  $\text{Ti}^{3+}$  has a  $g$ -value of 1.94–.99 [65,66]. Therefore, the signal at  $g=1.9766$  should be assigned to the  $\text{Ti}^{3+}$  species in OTA400. Batzill et al. reported that oxygen vacancies and related  $\text{Ti}^{3+}$  are always formed in the nitrogen-containing surface of common nitrogen-doped  $\text{TiO}_2$  [17]. In this study, with the addition of the IL, 3TA400 shows a stronger ESR signal at  $g=2.0042$ , indicating an increase in the oxygen vacancy. However, the signal at  $g=1.9766$  disappears, which seems to conflict with Batzill’s result. The removal of  $\text{Ti}^{3+}$  from the nitrogen-containing  $\text{TiO}_2$  (OTA400) confirmed that the above observation can be explained by the extra electrons provided by the doped boron that can effectively compensate for the charge difference between the substitutional  $\text{N}^{3-}$  and lattice  $\text{O}^{2-}$  (this can be understood according to the following defect equations:  $\text{B} + \text{Ti}^{4+} \rightarrow 1/\sigma \text{B}^{3+} + \text{Ti}^{3+}$ ;  $\text{Ti}^{3+} + \text{O}^{2-} + \text{N} \rightarrow \text{Ti}^{4+} + \text{N}^{3-} + \text{O}$ ) [30]. That is, no  $\text{Ti}^{3+}$  is present as a result of N-B-co-doping, which is a recombination center for photo-generated electrons and holes. It is also observed that the ESR signal decreases with the increase in calcination temperature, which is caused by the re-replacement of dopant atoms by O atoms during the calcination process under air atmosphere, as listed in Table 2.

### 3.5. UV-vis analysis

Usually, doping obviously influences the light absorption characteristics of the  $\text{TiO}_2$ . Therefore, the optical properties of the non-doped and doped  $\text{TiO}_2$  nanoparticles are measured by UV-Vis DRS. As displayed in Fig. 5a and Fig. S4, the absorption of P25 and

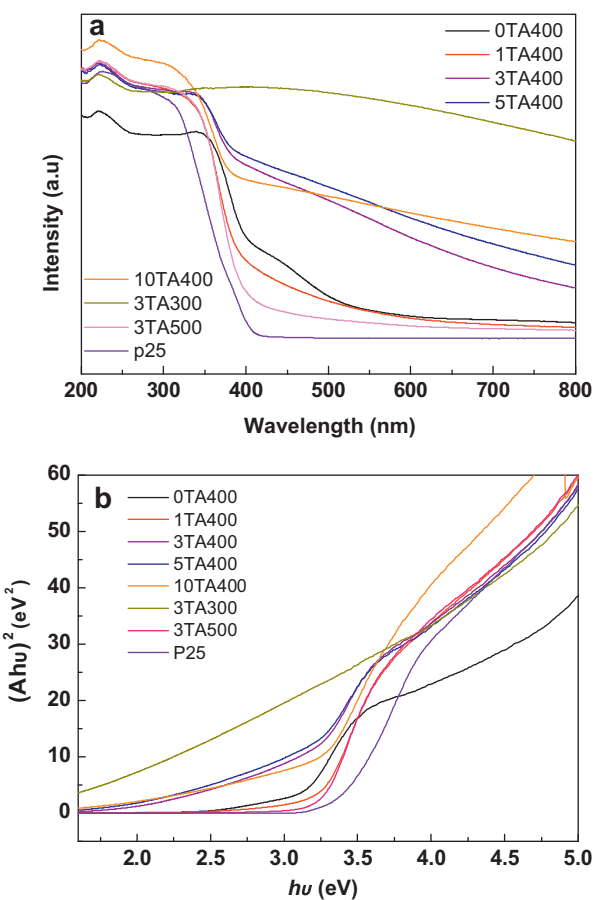


Fig. 5. UV-vis absorption spectra of samples.

ETA400 are limited only to the ultraviolet light region, while the absorption threshold values of the  $\text{TiO}_2$  nanoparticles prepared by  $\text{H}_2\text{TiO}_3$  are extended up to the visible light region. As representative samples, the appearance photographs of the samples 3TA80, 3TA300, 3TA400, 3TA500, and OTA400, are shown in Fig. S5, which are consistent with the DRS results. The band gap energies of the direct transition semiconductor can be calculated by a plot of  $(\alpha h\nu)^2$  versus the photon energy ( $h\nu$ ). The absorption coefficient  $\alpha$  and direct energy band gap ( $E_g$ ) of  $\text{TiO}_2$  are related through the following equation [67]:

$$\alpha(h\nu) = B(h\nu - E_g)^{1/2} \quad (1)$$

where  $\alpha$  represents the absorption coefficient,  $h$  is Planck’s constant, and  $\nu$  is the light frequency, and  $B$  is energy-independent constant. According to Eq. (1), the  $E_g$  of the resulting samples can be estimated from the plots of  $(\alpha h\nu)^2$  versus energy ( $h\nu$ ). The interception of the tangent to the  $X$  axis would give a good approximation of the  $E_g$  of the samples (Fig. 5b). The obtained  $E_g$  for the prepared  $\text{TiO}_2$  are shown in Table 1. The optical absorption edges of the nonmetal-doped samples shift to a lower energy region compared to those of P25 and ETA400. For the OTA400 sample without the IL, the absorption of the  $\text{TiO}_2$  particles also extended up to the visible light region, which was attributed to N doping from the addition of  $\text{NH}_3\text{H}_2\text{O}$  during the preparation. Owing to the addition of the IL, the absorption bands have a farther red shift to the visible spectral range. The red shift of the absorption bands in the visible spectral range for the F-doped  $\text{TiO}_2$  remains under debate. Yamaki et al. [68] and Li et al. [69] found that F doping alone did not cause the red shift of the absorption of  $\text{TiO}_2$ . They assumed that the F2p states were located below the bottom of the O2p valence band; therefore, F doping did

not affect the optical absorption property of the  $\text{TiO}_2$ . To investigate the influence of the F atoms on the absorption bands, 1-butyl-3-methylimidazolium trifluoroacetate ( $[\text{BMIm}]\text{AcF}_3$ ) was used as the reaction media and dopant in the preparation of N-F-co-doped  $\text{TiO}_2$  (without B). The DRS shown in Fig. S4 indicates that compared to that of OTA400, the energy band gap of the  $\text{TiO}_2$  obtained using  $[\text{BMIm}]\text{AcF}_3$  does not decrease. Thus, we propose that the synergistic effect of nitrogen and fluorine does not cause the red shift in the absorption of N- $\text{TiO}_2$  in this investigation.

Wu and co-workers found that B doping may lead to an increase in the formation of oxygen vacancies, which is responsible for the red-shifted optical absorption [70]. Some studies revealed that intrinsic defects, including those defects associated with oxygen vacancies, contribute to the absorption of light in the visible spectral region [71,72]. Kuznetsov and Serpone have proposed that the commonality in these anion-doped titanium species is in the formation of oxygen vacancies and the advent of color centers that absorb the visible light radiation [73]. Some reports have confirmed that F and B doping favors the formation of oxygen vacancies [23,58]. Therefore, we propose that the farther red shift of the IL-modified  $\text{TiO}_2$  is attributed to oxygen vacancies, which may be a result of the synergistic effect of N-B-F-tri-doping.

Fig. 5a also shows the absorption spectra of 3TA calcined at different temperatures. The visible light absorption of 3TA becomes weaker with the increase of the annealing temperature, suggesting that the annealing temperature has a great effect on the UV-vis absorption of 3TA. As shown in Fig. 5a, the carbonized IL is responsible for its strong visible light response, while 3TA was calcined at 300 °C. There is an evident blue shift to the UV light region when the annealing temperature increases to 500 °C. With the increase in temperature, the release of the doping nitrogen and fluorine is accelerated by oxidative reactions under the air atmosphere [74,75]. Thus, the amount of the doping nitrogen and fluorine in the  $\text{TiO}_2$  crystal is lower than that of the sample calcined at 400 °C, resulting in a blue shift to the UV light region.

### 3.6. Possible formation mechanism of doped $\text{TiO}_2$

As described in the experimental procedures, the reaction system became a homogeneous yellow-green solution after  $\text{H}_2\text{TiO}_3$  was added into an ice-cooled mixture of  $\text{H}_2\text{O}_2$  and  $\text{NH}_3\cdot\text{H}_2\text{O}$ . After the addition of the IL, the solution became more transparent, suggesting a soluble Ti-complex was formed. After microwave irradiation for 1 h, a yellow slurry formed, which was separated by filtration and dried at 80 °C to obtain 3TA80. To investigate the mechanism of the formation of the doped  $\text{TiO}_2$ , the raw IL and 3TA80 were characterized by FTIR. In the FTIR spectrum of  $[\text{BMIm}]\text{BF}_4$  (Fig. 6), the absorption bands at 1172, 1470 and 1573  $\text{cm}^{-1}$  are attributed to  $[\text{BMIm}]^+$ , and the absorption bands at 1061  $\text{cm}^{-1}$  are attributed to  $[\text{BF}_4]^-$  [38]. The weak absorption centered near 1650  $\text{cm}^{-1}$  is associated with the deformation vibration of the H–O–H bonds from the physisorbed water. A series of FTIR spectra of 3TA80 were obtained over time. In the initial stage,  $\text{H}_2\text{TiO}_3$  reacted with the mixture of  $\text{H}_2\text{O}_2$  and  $\text{NH}_3\cdot\text{H}_2\text{O}$  and then was converted to peroxotitanate [76]. With the addition of the IL, no obvious absorption bands associated with the ionic liquids were observed, which was because of the low concentration of the IL (Fig. 6b and c). At this stage, only a homogeneous yellow-green solution was obtained. After the microwave irradiation, the solution was transformed into a yellow slurry. As seen in Fig. 6d, a broad absorption in the range of 400–800  $\text{cm}^{-1}$  attributed to the vibration of Ti–O, indicating the rapid generation of  $\text{TiO}_2$  in the first 10 min. The absorption bands at approximately 1172, 1470 and 1573  $\text{cm}^{-1}$  were preserved in Fig. 6d and e, indicating the presence of trace  $[\text{BMIm}]^+$  at the surface of solid. However, the absorption band at approximately 1061  $\text{cm}^{-1}$  was split (Fig. 6d and e) and then

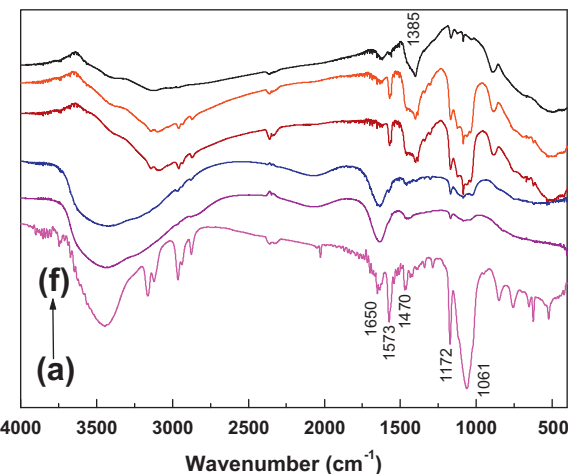


Fig. 6. FTIR spectra of  $[\text{BMIm}]\text{BF}_4$  and the  $\text{TiO}_2$  produced (a)  $[\text{BMIm}]\text{BF}_4$ , (b) peroxotitanate (solution), (c) peroxotitanate with IL (solution), (d) microwave irradiated 10 min (solid), (e) 20 min (solid) and (f) 60 min (solid).

disappeared (Fig. 6f), indicating the breakage of the  $[\text{BF}_4]^-$  bond during the microwave irradiation. Furthermore, at extended irradiation time (Fig. 6d–f), a new absorption band at 1385  $\text{cm}^{-1}$  was obtained, which indicated the present of a new chemical bond. As reported previously [76], the absorption peaks near 1385  $\text{cm}^{-1}$  could be assigned to B–N stretching vibrations. Because of the formation of B–N, the original B–F vibration was weakened and split.

On the basis of the experimental results, a possible mechanism for the formation of the doped nano- $\text{TiO}_2$  is proposed: at the early stage of the reaction process,  $\text{H}_2\text{TiO}_3$  reacted with the mixture of  $\text{H}_2\text{O}_2$  and  $\text{NH}_3\cdot\text{H}_2\text{O}$  and then was converted to peroxotitanate [76]. After adding the IL, the peroxotitanate reacted with  $[\text{BF}_4]^-$  to generate the B–N structure. Because the temperature rose rapidly as a result of the strong microwave absorption of the IL, fast decomposition of  $\text{H}_2\text{O}_2$  in peroxotitanate occurred, achieving the fast growth and cross-linking of the titanate [76]. Followed by the rapid growth of the titanate, some nano- $\text{TiO}_2$  crystals formed within several minutes. After calcination, amorphous  $\text{TiO}_2$  grew into crystals, and  $\text{NH}_3$  and the decomposed gas of the IL were released from the materials, leading to the formation of the mesoporous structure.

In the formation process, it is thought that  $[\text{BMIm}]^+$  interacts with bulk  $\text{TiO}_2$  through hydrogen bonds or electrostatic forces. Then, the nano- $\text{TiO}_2$  crystals are wrapped in the IL (see Fig. 1b). This process would induce the arrangement of the  $[\text{BF}_4]^-$  anions along the wall, which would pile up and stack, possibly through  $\pi$ – $\pi$  interactions or other noncovalent interactions between the imidazole rings [49]. Then, micelles would form. In this process, the IL played multiple roles. It not only served as the microwave absorbent but also as the dopant. Furthermore, the IL showed the ability to self-assemble under microwave irradiation, inhibiting the growth of the  $\text{TiO}_2$  crystals.

### 3.7. Photocatalytic activity

Fig. 7a shows the visible-light-induced photocatalytic decomposition of MO with different amounts of the IL dopant and ETA400. The photocatalytic reactions followed the Langmuir–Hinshelwood pseudo-first-order kinetics model when the initial dye concentrations of the reactants were low [51]. The kinetics equation can be expressed as follows:

$$\ln \frac{C_0}{C} = kt + \ln \frac{C_0}{C_1}$$

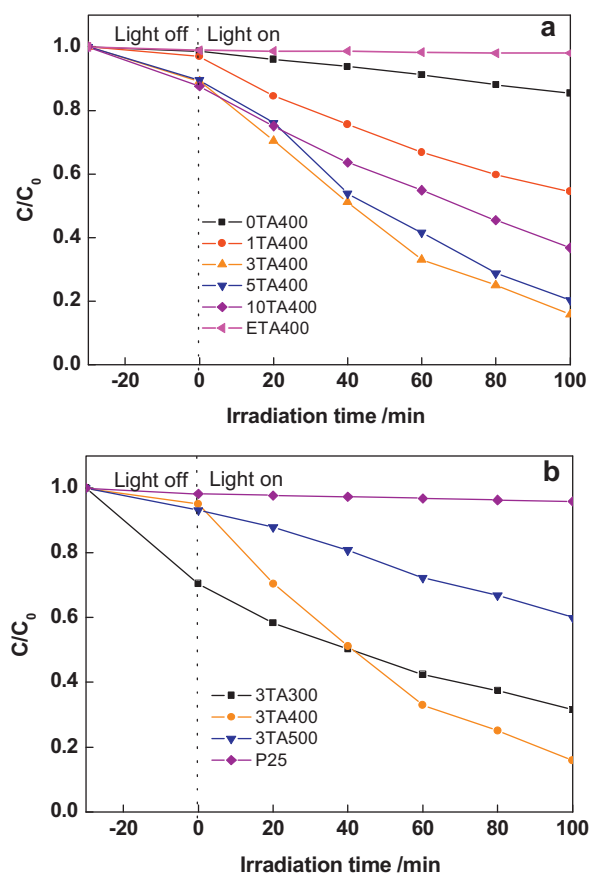


Fig. 7. Time-course variation of  $C/C_0$  for the MO solution over various samples.

where  $k$  is the pseudo-first-order rate constant,  $C_0$  is the original MO concentration (10 mg/L),  $C_1$  is the concentration after adsorption, and  $C$  is the concentration at reaction time  $t$ . The reaction rate constants  $k$  shown in Table 3 were determined to compare the photocatalytic abilities of these samples quantitatively. Almost no degradation of MO on ETA400 was observed under visible light irradiation. The degradation rate of MO on 0TA400 under visible light irradiation was also very low, which can be attributed to the fast recombination rate of the electron holes with N doping alone. The visible light photocatalytic activity of the IL-doped  $\text{TiO}_2$  is superior to that of 0TA400, ETA400, and commercial P25 for the degradation of MO. The reason for this result may be related to the synergistic effect of N–B–co-doping, which causes the absorption edge extension to the visible light range and, thus, plays an important role in improving the activity. When 3 g of the IL was added into this system, the photocatalytic activity of the prepared sample 3TA400 reached a maximum value of  $k$  of  $0.0173 \text{ min}^{-1}$ . The equation fitted for P25  $\text{TiO}_2$  is  $y = 0.00023x + 0.01823$ , where  $k$  is  $0.00023 \text{ min}^{-1}$ .

**Table 3**  
Pseudo-first-order kinetics for the photocatalytic degradation of MO with the various samples.

Sample	Fitted equation	Reaction rate constant, $k$ ( $\text{min}^{-1}$ )	Correlation coefficient, $R$
0TA400	$y = 0.0014x + 0.01415$	0.0014	0.9972
1TA400	$y = 0.0061x + 0.02065$	0.0061	0.9963
3TA400	$y = 0.0173x + 0.04975$	0.0173	0.9968
5TA400	$y = 0.0148x + 0.05648$	0.0148	0.9956
10TA400	$y = 0.0083x + 0.13225$	0.0083	0.9973
P25	$y = 0.00023x + 0.01823$	0.00023	0.9965
ETA400	$y = 0.000006x + 0.00011$	$10^{-6}$	0.9921
3TA300	$y = 0.0075x + 0.10635$	0.0075	0.9943
3TA500	$y = 0.0047x + 0.02457$	0.0047	0.9911

for P25, and the photocatalytic activity of 3TA400 is 75.2 times greater than that of P25 during the degradation of MO. In addition, an important step in the photocatalytic process is the adsorption of reacting substances onto the surface of the catalyst [45,77]. The mesoporous structure in the TA samples is good for the adsorption of pollutants. It is seen from  $\ln C_0/C_1$  in Table 3 that most of the TA samples showed higher absorption ability than that of P25. Generally, for a chemical reaction (except for zero-order reaction), an appropriate high absorption performance of catalyst to objective reactant is beneficial to its reaction rate.

Fig. S6 reveals a gradual decrease in the MO aqueous absorption under visible light irradiation. There is a blue shift for its maximum absorption wavelength, indicating there are intermediate products formed during MO degradation. The corresponding TOC removal of MO on 3TA400 at 100 min was 67.4%, which is lower than that of the degradation yield of 84.2%. This result shows that the mineralization is also not complete. However, when the amount of the IL exceeded 3 g, the photocatalytic activity of the samples decreased with an increasing amount of the IL, indicating that the excess N, B and F would become the recombination centers of the photo-induced electrons and holes, which is detrimental to photocatalytic reactions.

The influence of the calcination temperature on the degradation yield of MO is shown in Fig. 7b, and the reaction rate constants are shown in Table 3. It is known that both the crystal sizes and the states of the doped atoms have an influence on photocatalysis under visible light irradiation. As shown in Fig. 2 and Table 1, a higher calcination temperature induces the formation of a larger crystal size. Usually, the smaller the crystal size, the higher the activity of  $\text{TiO}_2$ . However, the performance of 3TA400 is better than that of 3TA300, although the latter has a smaller crystal size. However, the activity of 3TA400 is higher than that of 3TA500, which is due to the decrease of the doping elements in the  $\text{TiO}_2$  at higher calcination temperatures. In this case, the Ti–B–N structure acts as an efficient co-catalyst, which narrows the band gap by elevating the valence band edge. The presence of F ions physically adsorbed on the  $\text{TiO}_2$  surface can transfer the photo-induced electrons effectively. When the calcination temperature increases, the Ti–B–N structure is partly destroyed and the adsorbed F ions decrease (see Fig. 3b), which lowers the catalytic activity.

To investigate the universality of the prepared samples, RhB, OG and RX were selected as pollutants to evaluate the photocatalytic activity of 3TA400. The time-course variation of  $C/C_0$  for the dye solutions over samples 3TA400 and P25 and the rate constants  $k$  obtained are shown in Fig. S7 and Table S1, respectively. In comparison to P25, 3TA400 exhibits significantly enhanced photocatalytic activity for the decomposition of all the dyes under visible light. However, compared to the degradation of MO, P25 shows higher catalytic ability in the degradation of RX, RhB, and OG. The reason for this observation is that the dyes RX, RhB, and OG are photosensitive on P25 under visible light irradiation, while MO is not.

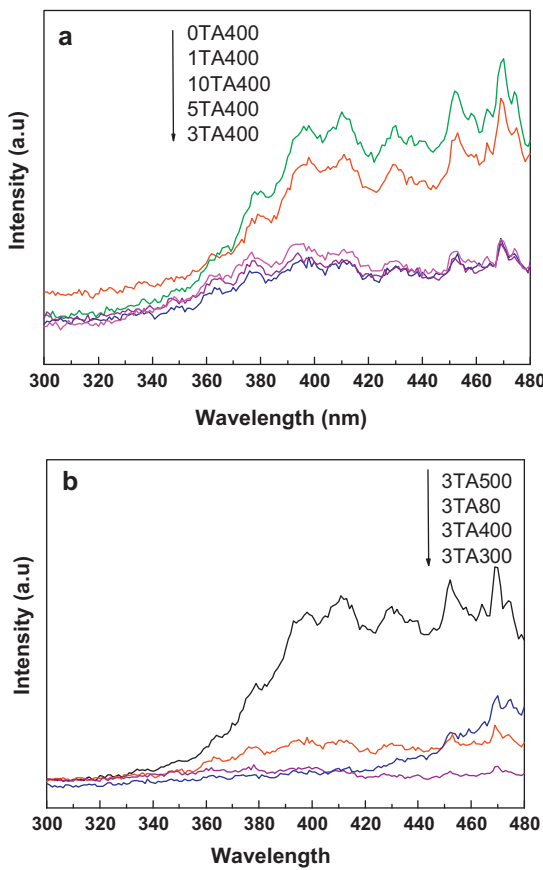


Fig. 8. Photoluminescence spectra of different samples.

Because 3TA400 exhibits the highest photocatalytic activity, the durability of the prepared photocatalysts and the surface oxygen defects were investigated. The cyclic stability tested on photocatalytic decomposition of MO is shown in Fig. S8. No significant decrease in its photocatalytic oxidation activity was observed after 6 uses. The surface oxygen defects of the recycled 3TA400 were detected by ESR (Fig. S9). The paramagnetic oxygen vacancy at  $g=2.004$  was obvious in these recycled samples (3 times and 6 times), indicating its highly stability in air.

### 3.8. PL analysis

PL emission spectra have been widely used to investigate the efficiency of charge carrier trapping, migration and transfer and to understand the fate of electron–hole pairs in semiconductor particles. It is known that PL emission results from the recombination of excited electrons and holes. A lower PL intensity may indicate a lower recombination rate of electron–holes under light irradiation [78]. Fig. 8a shows the PL spectra of TA400 with different amounts of the IL dopant. 0TA400 has the highest intensity among these samples, implying the fastest recombination rate of the electrons and holes. After the IL was introduced, the intensity of the PL emission decreased. This result indicates the recombination of charge carriers is effectively suppressed. It is reported that the formation of  $\text{Ti}^{3+}$  species in doped  $\text{TiO}_2$  may accelerate the recombination of photogenerated hole and electron pairs [60]. The synergistic effects of N and B doping hinder the conversion of the Ti species from  $\text{Ti}^{4+}$  to  $\text{Ti}^{3+}$ , which suppresses the recombination of charge carriers. In addition, the emission intensity is closely related to the calcination temperatures. As shown in Fig. 8b, the emission intensity of 3TA increased with increasing calcination temperatures. Combined with the XPS analysis, we think that the increase in the

photoluminescence intensity is the result of the replacement of N and F by O during the calcining process. Yu et al. found that because fluorine is the most electronegative element, its adsorption on the surface of  $\text{TiO}_2$  can attract photo-generated electrons and reduce the recombination rate of the photo-generated electrons and holes [79]. Cong et al. found that the doping of nitrogen in the  $\text{TiO}_2$  lattice led to the efficient quenching of the photoluminescence [80]. In this study, the effective quenching of the photoluminescence can be attributed to the synergistic effect of the dopant elements. One of the synergistic effects of B and N doping that hinders the conversion of Ti species from  $\text{Ti}^{4+}$  to  $\text{Ti}^{3+}$  is the suppression of the recombination of the charge carriers. Another is that the photo-generated electrons transferred on the conduction valance band can be attracted to the F adsorbed on the surfaces of  $\text{TiO}_2$ , which reduces the recombination rate of the photo-generated electrons and holes. Therefore, the synergistic effects of N–F–B-co-doping lead to improved electron–hole separation.

### 3.9. Photocatalytic mechanism of tri-doped $\text{TiO}_2$ under visible light irradiation

Liu et al. found that N–B-co-doping introduces more surface electronic states and changes the gaps between these states [26], which may have an important influence on the lifetime of the excitations. In this research, N, B and F are simultaneously doped in the  $\text{TiO}_2$ . The high visible light photocatalytic activity may be related to the synergistic effects of N–B–F-tri-doping. In the XPS spectra, the peaks at the BE of 190.5 eV for B1 s and 398.0 eV for N1 s verify the Ti–B–N bond. Furthermore, the doping of B2p and N2p states will effectively lead to decrease in the energy band gap of  $\text{TiO}_2$ .

In regards to the F doping, fluorine is the most electronegative element. It is adsorbed on the surfaces of  $\text{TiO}_2$  and can attract photo-generated electrons, which can reduce the recombination rate of the photo-generated electrons and holes, and improve the photocatalytic activity [79]. Minero et al. have reported that the surface modification of the  $\text{TiO}_2$  with fluorine results in the enhanced production of free  $\cdot\text{OH}$  radicals in solution [81]. In this study, Fig. 9a shows the  $\cdot\text{OH}$ -radical-trapping fluorescence spectra of the TA solution under visible light irradiation. The amounts of the  $\cdot\text{OH}$  radicals produced increases with increasing irradiation time. It is also observed that the highest amount of  $\cdot\text{OH}$  radicals are created over 3TA400. To further confirm the free  $\cdot\text{OH}$  radicals in solution, ESR/DMPO spin trapping experiments were also carried out to detect the  $\cdot\text{OH}$  radicals [48,82]. As shown in Fig. 9b, after visible light irradiation, the characteristic peaks of DMPO- $\cdot\text{OH}$  are observed for 3TA400, while the peaks of 0TA400 and 3TA500 are lower. The result of the ESR/DMPO spin trapping experiments is consistent with the fluorescence technique. These results demonstrate that the surface modification of  $\text{TiO}_2$  with fluorine can improve the separation efficiency of the electron–hole pairs and enhance the production of free  $\cdot\text{OH}$  radicals because there are more uncombined holes that can react with water or hydroxyl ions to form  $\cdot\text{OH}$  radicals.

To further investigate the effect of the F ions, another active species, the  $\cdot\text{O}_2^-$  anion, was also detected through ESR/DMPO spin trapping experiments using dimethyl sulphoxide (DMSO) as the solvent instead of water [48]. As shown in Fig. 9c,  $\cdot\text{O}_2^-$  signals are observed in 3TA400 and 3TA500, which demonstrate that adsorbed F ions did not obviously affect the formation of  $\cdot\text{O}_2^-$ . However, the  $\cdot\text{O}_2^-$  and  $\cdot\text{OH}$  signals in 0TA400 are all significantly lower than those in 3TA400 and 3TA500, which are due to the synergistic effect of N–B-codoping in 3TA.

To detect the main oxidative species in the photocatalytic process, radical and hole scavenger experiments were conducted using t-BuOH ( $\cdot\text{OH}$  scavenger),  $\text{AgNO}_3$  ( $e^-$  scavenger) and EDTA-2Na ( $h^+$  scavenger) [83,84]. As shown in Fig. 10, in the 3TA400 system,

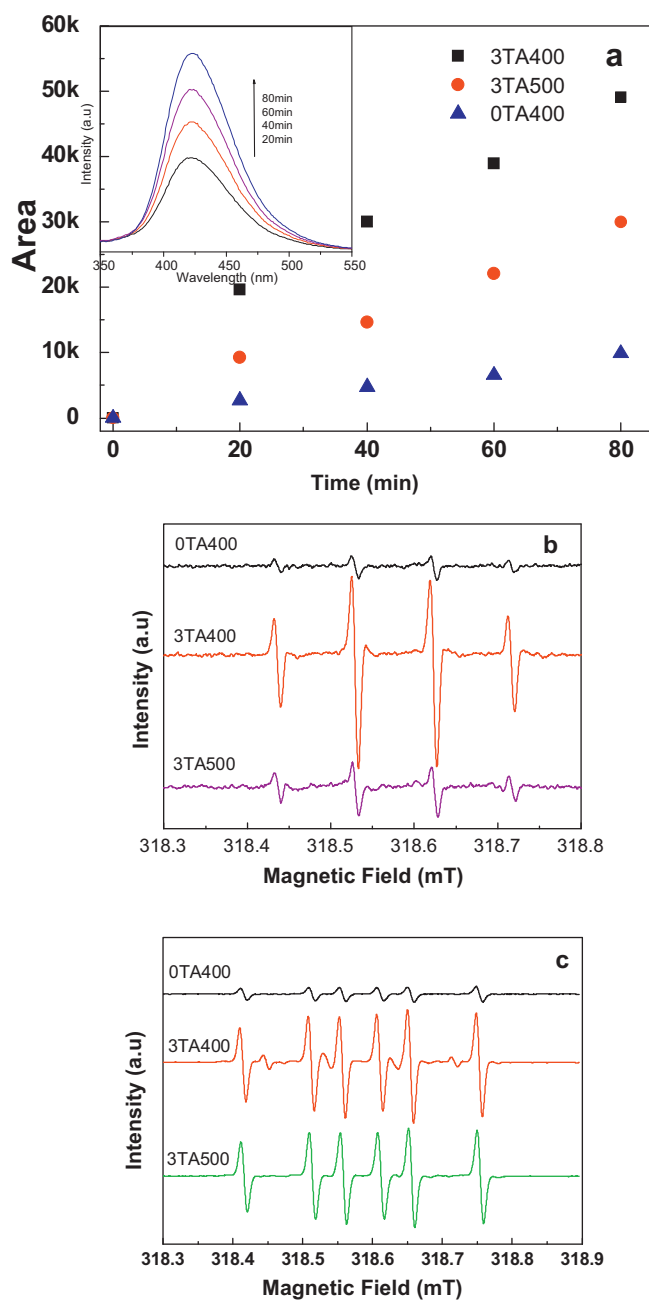


**Fig. 9.** (a) Plots of the induced fluorescence peak area at 426 nm irradiation for TA on different samples, (b) ESR spectra of DMPO-•OH adducts after irradiation for 5 min and (c) ESR spectra of DMPO-•O<sup>2-</sup> adducts after irradiation for 5 min.

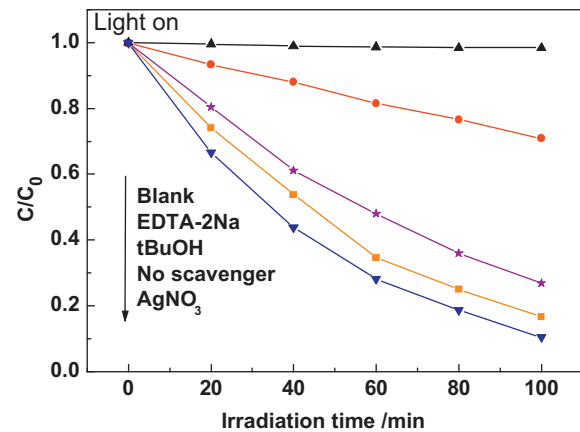
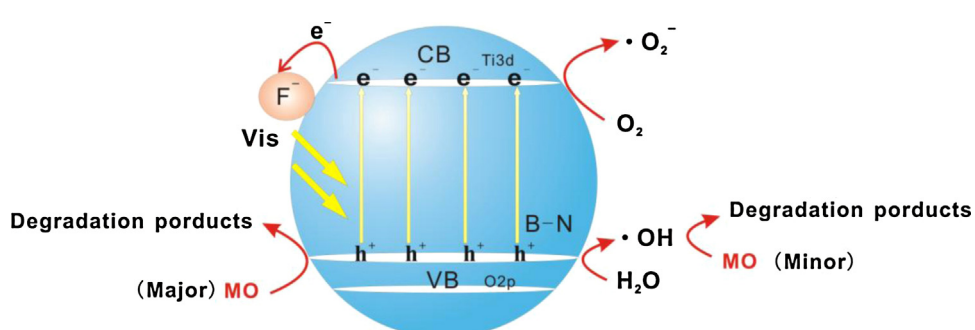
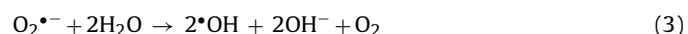


**Fig. 10.** Time course of the  $C/C_0$  of MO over the prepared 3TA400 photocatalyst in the presence of various radical scavengers.

the addition of t-BuOH only causes a small decline in the photo-degradation of MO. On the contrary, the addition of EDTA-2Na suppresses the photocatalytic activity of 3TA400 greatly. Moreover, AgNO<sub>3</sub> has a small accretion effect on the photo-degradation of MO. The results suggest that the holes are the main oxidative species, •OH radicals are the minor reactive species, and •O<sup>2-</sup> has no effect on the degradation of MO.

There are two routes to obtain •OH radicals, as shown in Eqs. (1) and (3). In this study, the results that addition of AgNO<sub>3</sub> as electrons scavenger improved the catalytic efficiency and that the almost same •O<sup>2-</sup> amount did not generate same •OH amount shown in Fig. 9 indicate that •OH radicals should not be generated through Eqs. (1) and (2). On the other hand, the valence band edge potentials of N 2p are located at 2.45–2.70 eV calculated from the Eg of doped TiO<sub>2</sub> (2.75–3.00 eV) and the conductive band of Ti3d (−0.30 eV), which are more positive than the standard reduction potential of •OH/H<sub>2</sub>O (2.27 eV) [85], indicating the h<sup>+</sup> can react with H<sub>2</sub>O adsorbed on the surface of catalysts to produce •OH radical (shown as Eq. (3)), which is consistent with previous researches [86,87]. Based on the results presented above, the proposed mechanism for the photocatalytic degradation of MO under visible light is shown in Scheme 1.



**Scheme 1.** Possible visible light photocatalytic mechanism for the synergistic effect of N-B-F-tri-doped TiO<sub>2</sub>.

#### 4. Conclusions

A facile and green method was developed for the simultaneous doping of nitrogen, boron and fluorine in  $\text{TiO}_2$  by  $\text{H}_2\text{TiO}_3$  via a microwave-assisted route. In addition to the reaction media (including the microwave absorbent), the ionic liquid (IL) [ $\text{BMIm}$ ]BF<sub>4</sub> served as the dopant. N doping occurred through the addition of  $\text{NH}_3\cdot\text{H}_2\text{O}$ , and B and F originated from the [ $\text{BMIm}$ ]BF<sub>4</sub> IL. Furthermore, the IL also displayed the ability to self-assemble under microwave irradiation, which made it an inhibitor of the growth of the  $\text{TiO}_2$  particles. As a result, the  $\text{TiO}_2$  obtained exhibited small crystal size, high BET surface area and a mesoporous structure, which are beneficial to the adsorption of pollutants on the surface of the photocatalysts as well as the photocatalytic activity. In the preparation method, the optimum weight ratio of the IL to  $\text{H}_2\text{TiO}_3$  was 3:1, and the calcination temperature was 400 °C. Under the experimental conditions, the N–B–F-tri-doped  $\text{TiO}_2$  obtained exhibited the highest photocatalytic ability in the decomposition of methylene blue under visible light irradiation, which was 75.2 times greater than that of commercial P25  $\text{TiO}_2$ , as evaluated using pseudo-first-order kinetics rate constants. The doped  $\text{TiO}_2$  also exhibit excellent visible light photocatalytic activity in degradation of rhodamine B, Orange G, and reactive red X. The enhanced visible-light activity mainly originated from the synergistic effects N–B–F-tri-doping and the large specific surface area. N–B-co-doping decreased the band gap of the  $\text{TiO}_2$  from 3.2 eV to 2.78 eV, which facilitated its absorption of visible light. F-doping benefited the electron transfer in the process. The large specific surface areas caused by the inhibition of the IL on the growth of the  $\text{TiO}_2$  crystals in the calcination process improved the adsorption of the pollutants. These factors resulted in excellent visible-light photocatalytic activity for the N–B–F-tri-doped  $\text{TiO}_2$  catalysts prepared. This study presents a simple strategy further to improve the visible-light activity and quantum yield of  $\text{TiO}_2$  using an IL. We hope that this study can contribute to photocatalysis research and presents a new application of ILs in the preparation of nanomaterials.

#### Acknowledgments

This work was supported by the National Natural Science Foundation of China (No. 21076060, 20806021), the Program for New Century Excellent Talents in University (NCET-12-0686), the Key Project of Chinese Ministry of Education (No. 210018), the One-Hundred Outstanding Innovative Talents Scheme of Hebei Province Education Department (No. CPRC022), and the Research Foundation of Hebei Province Education Department (No. Z2012069).

#### Appendix A. Supplementary data

Supplementary data associated with this article can be found, in the online version, at <http://dx.doi.org/10.1016/j.apcatb.2013.07.050>.

#### References

- [1] T. Ochiai, A. Fujishima, *Journal of Photochemistry and Photobiology C* 13 (2012) 247.
- [2] J.L. Zhang, Y.M. Wu, X.M. Yang, S.A.K. Leghari, S. Sajjad, *Energy & Environmental Science* 3 (2010) 715.
- [3] R. Asahi, T. Morikawa, T. Ohwaki, K. Aoki, Y. Taga, *Science* 293 (2001) 269.
- [4] G.B. Soares, B. Bravim, C.M.P. Vaz, C. Ribeiro, *Applied Catalysis B* 106 (2011) 287.
- [5] J. Wang, D.N. Tafen, J.P. Lewis, Z.L. Hong, A. Manivannan, M.J. Zhi, M. Li, N.Q. Wu, *Journal of the American Chemical Society* 131 (2009) 12290.
- [6] X.F. Chen, X.C. Wang, Y.D. Hou, J.H. Huang, L. Wu, X.Z. Fu, *Journal of Catalysis* 255 (2008) 59.
- [7] Y. Huang, W.K. Ho, Z.H. Ai, X.A. Song, L.Z. Zhang, S.C. Lee, *Applied Catalysis B* 89 (2009) 398.
- [8] D. Chen, D. Yang, Q. Wang, Z.Y. Jiang, *Industrial and Engineering Chemistry Research* 45 (2006) 4110.
- [9] X.D. Wang, M. Blackford, K. Prince, R.A. Caruso, *ACS Applied Materials & Interfaces* 4 (2012) 476.
- [10] Y. Park, W. Kim, H. Park, T. Tachikawa, T. Majima, W. Choi, *Applied Catalysis B* 91 (2009) 355.
- [11] C. Han, M. Pelaez, V. Likodimos, A.G. Kontos, P. Falaras, K. O'Shea, D.D. Dionysiou, *Applied Catalysis B* 107 (2011) 77.
- [12] H.M. Yang, X.C. Zhang, *Journal of Materials Chemistry* 19 (2009) 6907.
- [13] A.M. Czoska, S. Livraghi, M. Chiesa, E. Giamello, S. Agnoli, G. Granozzi, E. Finazzi, C. Di Valentini, G. Pacchioni, *Journal of Physical Chemistry C* 112 (2008) 8951.
- [14] M.M. Khin, A.S. Nair, V.J. Babu, R. Murugan, S. Ramakrishna, *Energy & Environmental Science* 5 (2012) 8075.
- [15] N.I. Serpone, *Journal of Physical Chemistry B* 110 (2006) 24287.
- [16] G. Liu, L.Z. Wang, H.G. Yang, H.M. Cheng, G.Q. Lu, *Journal of Materials Chemistry* 20 (2010) 831.
- [17] M. Batzill, E.H. Morales, U. Diebold, *Physical Review Letters* 96 (2006) 026103.
- [18] Y. Komai, K. Okitsu, R. Nishimura, N. Ohtsu, G. Miyamoto, T. Furuhara, S. Semboishi, Y. Mizukoshi, N. Masahashi, *Catalysis Today* 164 (2011) 399.
- [19] J.A. Rengifo-Herrera, K. Pierzchala, A. Sienkiewicz, L. Forro, J. Kiwi, C. Pulgarin, *Applied Catalysis B* 88 (2009) 398.
- [20] P. Xu, T. Xu, J. Lu, S.M. Gao, N.S. Hosmane, B.B. Huang, Y. Dai, Y.B. Wang, *Energy & Environmental Science* 3 (2010) 1128.
- [21] D. Dolat, N. Quici, E. Kusiak-Nejman, A.W. Morawski, G.L. Puma, *Applied Catalysis B* 115 (2012) 81.
- [22] A.E. Giannakas, E. Seristatidou, Y. Deligiannakis, I. Konstantinou, *Applied Catalysis B* 132 (2013) 460.
- [23] Y.M. Wu, M.Y. Xing, B.Z. Tian, J.L. Zhang, F. Chen, *Chemical Engineering Journal* 162 (2010) 710.
- [24] X. Zong, Z. Xing, H. Yu, Z.G. Chen, F.Q. Tang, J. Zou, G.Q. Lu, L.Z. Wang, *Chemical Communications* 47 (2011) 11742.
- [25] Q.C. Xu, Y. Zhang, Z.M. He, S.C.J. Loo, T.T.Y. Tan, *Journal of Nanoparticle Research* 14 (2012) 1042.
- [26] G. Liu, Y.N. Zhao, C.H. Sun, F. Li, G.Q. Lu, H.M. Cheng, *Angewandte Chemie International Edition* 47 (2008) 4516.
- [27] A.M. Czoska, S. Livraghi, M.C. Paganini, E. Giamello, C. Di Valentini, G. Pacchioni, *Physical Chemistry Chemical Physics* 13 (2011) 136.
- [28] N. Shi, X.H. Li, T.X. Fan, H. Zhou, J. Ding, D. Zhang, H.X. Zhu, *Energy & Environmental Science* 4 (2011) 172.
- [29] P.H. Wang, P.S. Yap, T.T. Lim, *Applied Catalysis A* 399 (2011) 252.
- [30] G. Liu, L.C. Yin, J.Q. Wang, P. Niu, C. Zhen, Y.P. Xie, H.M. Cheng, *Energy & Environmental Science* 5 (2012) 9603.
- [31] F. Li, X.L. Yin, M.M. Yao, J. Li, *Journal of Nanoparticle Research* 13 (2011) 4839.
- [32] H. Irie, Y. Watanabe, K. Hashimoto, *Journal of Physical Chemistry B* 107 (2003) 5483.
- [33] M. D'Arienzo, R. Scotti, L. Wahba, C. Battocchio, E. Bemporad, A. Nale, F. Morazzone, *Applied Catalysis B* 93 (2009) 149.
- [34] D.M. Chen, Z.Y. Jiang, J.Q. Geng, J.H. Zhu, D. Yang, *Journal of Nanoparticle Research* 11 (2009) 303.
- [35] O. Diwald, T.L. Thompson, T. Zubkov, E.G. Goralski, S.D. Walck, J.T.J. Yates, *Journal of Physical Chemistry B* 108 (2004) 6004.
- [36] H.H. Ou, S.L. Lo, C.H. Liao, *Journal of Physical Chemistry C* 115 (2011) 4000.
- [37] M. Baghbanzadeh, L. Carbone, P.D. Cozzoli, C.O. Kappe, *Angewandte Chemie International Edition* 50 (2011) 11312.
- [38] K.L. Ding, Z.J. Miao, Z.M. Liu, Z.F. Zhang, B.X. Han, G.M. An, S.D. Miao, Y. Xie, *Journal of the American Chemical Society* 129 (2007) 6362.
- [39] X.J. Wang, F.T. Li, J.X. Liu, C.G. Kou, Y. Zhao, Y.J. Hao, D.S. Zhao, *Energy & Fuels* 26 (2012) 6777.
- [40] W.M. Xuan, C.F. Zhu, Y. Liu, Y. Cui, *Chemical Society Reviews* 41 (2012) 1677.
- [41] Z.X. Li, J.C. Barnes, A. Bosoy, J.F. Stoddartbc, J.I. Zink, *Chemical Society Reviews* 41 (2012) 2590.
- [42] V.B.R. Boppana, R.F. Lobo, *Journal of Catalysis* 281 (2011) 156.
- [43] J.G. Yu, Y.R. Su, B. Cheng, *Advanced Functional Materials* 17 (2007) 1984.
- [44] K. Ariga, A. Vinu, Y. Yamauchi, Q.M. Ji, J.P. Hill, *Bulletin of the Chemical Society of Japan* 85 (2012) 1.
- [45] Y. Li, Z.Y. Fu, B.L. Su, *Advanced Functional Materials* 22 (2012) 4634.
- [46] K.I. Ishibashi, A. Fujishima, T. Watanabe, K. Hashimoto, *Electrochemistry Communications* 2 (2000) 207.
- [47] F.T. Li, Y. Liu, Z.M. Sun, Y. Zhao, R.H. Liu, L.J. Chen, D.S. Zhao, *Catalysis Science & Technology* 2 (2012) 1455.
- [48] M.G. Yin, Z.S. Li, J.H. Kou, Z.G. Zou, *Environmental Science and Technology* 43 (2009) 8361.
- [49] Y. Liu, J. Li, M.J. Wang, Z.Y. Li, H.T. Liu, P. He, X.R. Yang, H. Li, *Crystal Growth and Design* 5 (2005) 1643.
- [50] S. Brunauer, P.H. Emmet, E. Teller, *Journal of the American Chemical Society* 62 (1940) 1723.
- [51] F.T. Li, Y. Zhao, Y.J. Hao, X.J. Wang, R.H. Liu, D.S. Zhao, D.M. Chen, *Journal of Hazardous Materials* 239/240 (2012) 118.
- [52] S. Livraghi, K. Elghniji, A.M. Czoska, M.C. Paganini, E. Giamello, M. Ksibi, *Journal of Photochemistry and Photobiology A* 205 (2009) 93.
- [53] F. Wei, L. Ni, P. Cui, *Journal of Hazardous Materials* 156 (2008) 135.
- [54] X. Wang, T.T. Lim, *Applied Catalysis B* 100 (2010) 355.
- [55] G. Liu, C.H. Sun, L.N. Cheng, Y.G. Jin, H.F. Lu, L.Z. Wang, S.C. Smith, G.Q. Lu, H.M. Cheng, *Journal of Physical Chemistry C* 113 (2009) 12317.
- [56] C.D. Wagner, W.M. Riggs, L.E. Davis, J.F. Moulder, G.E. Muilenberg (Eds.), *Handbook of X-ray Photoelectron Spectroscopy*, PerkinElmer Co., MN, 1979.
- [57] S. In, A. Orlov, R. Berg, F. García, S.P. Jimenez, M.S. Tikhov, D.S. Wright, R.M. Lambert, *Journal of the American Chemical Society* 129 (2007) 13790.

[58] Y.M. Wu, M.Y. Xing, J.L. Zhang, F. Chen, *Applied Catalysis B* 97 (2010) 182.

[59] Y. Huo, X. Zhang, Y. Jin, J. Zhu, H. Li, *Applied Catalysis B* 83 (2008) 78.

[60] E. Finazzi, C.D. Valentini, G. Pacchioni, *Journal of Physical Chemistry C* 113 (2009) 220.

[61] N. Feng, A. Zheng, Q. Wang, P. Ren, X. Gao, S.B. Liu, Z. Shen, T. Chen, F. Deng, *Journal of Physical Chemistry C* 115 (2011) 2709.

[62] G.D. Tang, Z. Jiang, H.H. Shi, T.C. Xiao, Z.F. Yan, *Journal of Materials Chemistry* 20 (2010) 5301.

[63] S.K. Joung, T. Amemiya, M. Murabayashi, K. Itoh, *Chemistry – A European Journal* 12 (2006) 5526.

[64] N.M. Dimitrijevic, Z.V. Sapomjic, B.M. Rabatic, O.G. Poluektov, T. Rajh, *Journal of Physical Chemistry C* 111 (2007) 14597.

[65] J.C. Conesa, J. Soria, *Journal of Physical Chemistry* 86 (1982) 1392.

[66] I. Nakamura, N. Negishi, S. Kutsuna, T. Ihara, S. Sugihara, K. Takeuchi, *Journal of Molecular Catalysis A* 161 (2000) 205.

[67] J. Tauc, *Materials Research Bulletin* 5 (1970) 721.

[68] T. Yamaki, T. Umebayashi, T. Sumita, S. Yamamoto, M. Maekawa, A. Kawasuso, H. Itoh, *Physics Research B* 206 (2003) 254.

[69] D. Li, H. Haneda, S. Hishita, N. Ohashi, *Chemistry of Materials* 17 (2005) 2596.

[70] Y.M. Wu, M.Y. Xing, J.L. Zhang, *Journal of Hazardous Materials* 192 (2011) 368.

[71] Z. Lin, A. Orlov, R.M. Lambert, M.C. Payne, *Journal of Physical Chemistry B* 109 (2005) 20948.

[72] I.N. Martyanov, S. Uma, S. Rodrigues, K.J. Klabunde, *Chemical Communications* 21 (2004) 2476.

[73] V.N. Kuznetsov, N. Serpone, *Journal of Physical Chemistry C* 113 (2009) 15110.

[74] M. Sathish, B. Viswanathan, R.P. Viswanath, C.S. Gopinath, *Chemistry of Materials* 17 (2005) 6349.

[75] Y.X. Li, G.F. Ma, S.Q. Peng, G.X. Lu, S.B. Li, *Applied Surface Science* 254 (2008) 6831.

[76] Y.F. Gao, M. Nagai, *Journal of the American Ceramic Society* 90 (2007) 831.

[77] G. Peccati, P. Reyes, P. Sanhueza, J. Villasenor, *Chemosphere* 43 (2001) 141.

[78] K. Nagaveni, M.S. Hegde, G. Madras, *Journal of Physical Chemistry B* 108 (2004) 20204.

[79] J.C. Yu, W.G. Wang, B. Cheng, B.L. Su, *Journal of Physical Chemistry C* 113 (2009) 6743.

[80] Y. Cong, J.L. Zhang, F. Chen, M. Anpo, *Journal of Physical Chemistry C* 111 (2007) 6976.

[81] C. Minero, G. Mariella, V. Maurino, D. Vione, E. Pelizzetti, *Langmuir* 16 (2000) 8964.

[82] H. Fu, L. Zhang, S. Zhang, Y. Zhu, *Journal of Physical Chemistry B* 110 (2006) 3061.

[83] Y.J. Wang, R. Shi, J. Lin, Y.F. Zhu, *Energy & Environmental Science* 4 (2011) 2922.

[84] Y.N. Huo, J. Zhang, M. Miao, Y. Jin, *Applied Catalysis B* 111/112 (2012) 334.

[85] A. Fujishima, X.T. Zhang, *Comptes Rendus Chimie* 9 (2006) 750.

[86] G.D. Yang, Z. Jiang, H.H. Shi, T.C. Xiao, Z.F. Yan, *Journal of Materials Chemistry* 20 (2010) 5301.

[87] D.H. Wang, L. Jia, X.L. Wu, L.Q. Lu, A.W. Xu, *Nanoscale* 4 (2012) 576.